Marine Geology 500 (2026) 107839

Contents lists available at ScienceDirect

Marine Geology

journal homepage: www.elsevier.com/locate/margo

Research Article

Tracking sedimentation process under progressive mangrove propagation in low-energy bays

Weiming Li [a], Zhijun Dai [a,b,*], Xuefei Mei [a,c], Jiejun Luo [a], Wenjun Zeng [a], Ping Zhang [a], Ran Chen [a], Jinping Cheng [c,*]

[a] State Key Laboratory of Estuarine and Coastal Research, East China Normal University, Shanghai 200241, China
[b] Laboratory for Marine Geology, Qingdao Marine Science and Technology Center, Qingdao, China
[c] Department of Science and Environmental Studies, The Education University of Hong Kong, New Territories, Hong Kong, China

ARTICLE INFO

Editor: Nadia Senechal

Keywords:
Mangrove wetland
Seaward expansion
sediment accumulation
Coastal resilience
Climate change

ABSTRACT

Mangroves play a critical role in wave attenuation, carbon storage and tidal flat accretion. However, the mechanisms linking mangrove sedimentation to tidal flat deposition environment were not well documented. This study reconstructed the historical sedimentation process of the Mai Po Mangrove Reserve, a low-energy system with limited human disturbance, using in situ observations, sediment core samples and remote sensing images. The results show that sediments at the seaward mangrove fringe experienced two coarsening phases during 1990–2024, with mean grain size decreasing from 6.58 ± 0.77 φ before 2006 to 5.80 ± 0.66 φ after 2006 and further to 5.20 ± 0.65 φ after 2017. Within the mangrove interior, mean grain size increased from 3.35 ± 0.38 φ to 5.14 ± 0.95 φ after 1996, and subsequently decreased to 3.96 ± 0.39 φ after 2017, remaining consistently coarser than the fringe. Meanwhile, the mass accumulation rate (MAR) declined markedly from 1.40 g cm^{-2} yr^{-1} in 1999 to 0.94 g cm^{-2} yr^{-1} in 2016 and then sharply rebounded to 1.31 ± 0.07 g cm^{-2} yr^{-1}, whereas MAR within the interior steadily decreased, with a mean value of 0.54 ± 0.12 g cm^{-2} yr^{-1} over the study period, consistently lower than the fringe. The seaward expansion of northern mangroves intercepted tidal and fluvial sediments before they reached the sampling sites, driving sediment coarsening and the initial MAR decline. In contrast, Shenzhen River regulation enhanced fine sediment supply to the mangrove interior, leading to early-stage fining. Weaker hydrodynamic forcing and shorter hydroperiods maintained lower sediment accumulation in the interior. Additionally, occasional typhoon events triggered sediment coarsening in both zones, while sea-level rise exerted only minor influence. These findings provide a theoretical basis for resilience evaluation of mangrove wetland systems and the protection and restoration policy setting.

1. Introduction

Mangroves thrive in the intertidal zones of tropical and subtropical regions, where they experience periodic inundation due to tidal fluctuations (Jia et al., 2019; Xia et al., 2018; Quadros et al., 2021). Mangrove ecosystems are widely recognized as among the most productive on Earth, with their primary productivity rivaling that of tropical rainforests. Notably, mangroves store even greater amounts of carbon, primarily sequestered in the soil (Alongi, 2025; Alongi, 2014). Furthermore, mangrove ecosystems provide a multitude of critical ecosystem services, including coastal protection, water purification, fish biomass production, and habitat provision. Collectively, these ecosystem services exceed those of many other coastal blue carbon systems in both ecological and economic value, emphasizing the essential role of mangroves as natural buffers that enhance coastal resilience and warrant their integration into sustainable management frameworks (Duarte and Cebrián, 1996; Trégarot et al., 2021; Anu et al., 2024).

A core underpinning of these services is the capacity of mangroves to trap, stabilize, and accrete sediments. Their complex root architectures (e.g., prop roots, pneumatophores) reduce flow velocities, dissipate wave energy, and facilitate sediment deposition and retention of fine particles—especially silt, clay, and allochthonous organic matter (Sánchez-Núñez et al., 2019). These processes reinforce substrate stability and help maintain shoreline integrity (Karimi et al., 2022). Sediments also act as vectors for contaminants that are intercepted and

* Corresponding authors.
E-mail addresses: zjdai@sklec.ecnu.edu.cn (Z. Dai), jincheng@eduhk.hk (J. Cheng).

https://doi.org/10.1016/j.margeo.2026.107839
Received 24 October 2025; Received in revised form 25 June 2026; Accepted 29 June 2026
Available online 30 June 2026

deposited within mangrove substrate, thereby contributing to water purification (Liu et al., 2022). Concurrently, sediment deposition delivers, sediment deposition also delivers substantial amounts of organic matter and nutrients through physical, chemical, and biological pathways (Liu et al., 2022; Nguyen et al., 2025), while sedimentary microbial communities facilitate organic matter degradation, supporting mangrove productivity and improving water quality (Sarker et al., 2021). Critically, sediment trapping increases surface elevation, a key mechanism by which mangroves keep pace with sea-level rise (Lovelock et al., 2015). Accretion and associated intertidal elevation gains promote seaward expansion and the maintenance of coupled mangrove–mudflat systems that provide essential habitat and food resources for marine biota (van Maanen et al., 2015; Woodroffe et al., 2016; Meijer et al., 2021).

Sediment availability and redistribution within mangroves are governed by local hydrodynamics, including tidal flows, river discharge, and waves. During flood tides, suspended sediments are transported into mangrove forests, where vegetation-induced drag enhances settling and retention (Jiang et al., 2025). In estuarine settings, riverine inputs are major sediment sources; fluvial sediments are subsequently sorted and redistributed by tides, with coarser fractions often delivered to mangrove (Allison et al., 1995). Over longer timescales, persistent riverine sediment supply can drive seaward progradation of mangrove margins (Vundavilli et al., 2024). Wave activity further modulates sediment dynamics by increasing the concentration of suspended sediments and enhancing transport capacity; as waves penetrate vegetated zones, rapid energy attenuation promotes fine-sediment deposition (Hong Phuoc and Massel, 2006; Gijsman et al., 2024). Beyond these local drivers, episodic typhoons can alter mangrove sedimentation through storm surges, while the ongoing rise in sea level is expected to impose a more persistent hydrodynamic influence on sediment dynamics (Feher et al., 2020; Sanders et al., 2012).

Previous studies have yielded inconsistent results regarding the relationship between sedimentation in mangrove and non-mangrove areas (Pérez et al., 2018; Pérez et al., 2021; Sanders et al., 2010a; Dung et al., 2023). Hydrodynamic forcing has been identified as a key factor controlling these differences (Pérez et al., 2018). A synthesis of existing studies reveals a clear pattern linked to hydrodynamic conditions (Table S1). Under relatively high-energy hydrodynamic conditions, sedimentation rates in adjacent mudflats are generally lower than those within mangrove forests, sometimes as low as one-eighth of the rates observed in mangrove areas (Hongwiset et al., 2022). In contrast, under lower-energy settings, the opposite pattern has been reported, with mudflat sedimentation rates reaching about 2.6 times those within mangroves at Tamandaré, Brazil (Sanders et al., 2010b). However, in many studies described above, hydrodynamic influences were inferred indirectly from qualitative observations or geomorphic and ecological proxies, such as sedimentary facies, vegetation structure, and surface elevation, rather than measured directly. Although these approaches provide useful insights, they introduce uncertainties and potential biases, limiting the ability to attribute sedimentation patterns to specific flow dynamics.

Mangrove sediment dynamics vary widely depending on the dominant hydrodynamic forcing (Woodroffe et al., 2016; Zhou et al., 2024; Sánchez-Núñez et al., 2019; Wang et al., 2025). As summarized in Table S2, river-dominated mangrove systems generally exhibit higher sedimentation rates due to abundant fluvial sediment supply, and their deposits are typically enriched in fine-grained materials such as clay and silt. In contrast, tide-dominated systems are characterized by intermediate sedimentation rates and are strongly influenced by tidal exchange processes, often displaying pronounced spatial heterogeneity in both sedimentation patterns and grain-size composition, although fine sediments such as clay and silt still tend to dominate depositional zones. Wave-dominated mangrove environments exhibit the lowest sedimentation rates among the three settings and are primarily shaped by erosion and sediment reworking, resulting in comparatively coarser sediments with a higher proportion of sand due to strong hydrodynamic energy and limited retention of fine particles. Although the Mai Po mangrove is situated in a tide-dominated estuary (Yang and Chui, 2017), it is also affected by riverine inputs from the Shenzhen River, making it a representative case for examining how hydrodynamic forces regulate sedimentation patterns in tide-influenced estuarine mangroves. This study therefore aims to 1) quantify spatial variations in grain size and sedimentation rates between the mangrove fringe and interior of the Mai Po mangroves; and 2) examine the potential drivers of these variations, with particular emphasis on hydrodynamic forcing. To overcome the biases and uncertainties in estimating hydrodynamic effects associated with reliance on indirect proxies, unlike previous studies, direct in situ hydrodynamic measurements combined with analyses of suspended sediments, sediment cores, and radiometric ages are employed to robustly link short-term flow dynamics with longer-term sediment accumulation. By explicitly accounting for spatial heterogeneity between the mangrove fringe and interior and incorporating extreme events, a process-based understanding of the mechanisms controlling sedimentation in tide-influenced mangroves is achieved. Based on the integration of multiple datasets from the tide-influenced Mai Po mangroves, a framework is developed to understand how hydrodynamic forcing controls sediment dynamics through in situ observations, thereby providing a process-based, mechanistic explanation of sediment variability and its key controlling factors in mangrove tidal flats. This framework may provide useful insights for understanding estuarine mangroves and tidal flats and could potentially inform future conservation and restoration planning.

2. Materials and methods

2.1. Study area

Deep Bay is situated precisely at the border between Hong Kong and Guangdong, and represents a region of both ecological and geographical significance (Fig. 1A). As part of the Pearl River Estuary and a semi-enclosed tidal lagoon-type bay, Deep Bay is strongly influenced by Pearl River discharge, with 50–80% of its mouth's water volume originating from the river during peak conditions (Yang and Chui, 2021). Although Deep Bay is a tide-dominated system with semi-diurnal tides and an average tidal range of about 1.7 m, the inner bay exhibits relatively weak hydrodynamic energy (Yang and Chui, 2017), which in turn influences sediment transport processes. Sediment is supplied from both riverine and tidal sources, though the latter dominates. Moreover, limited water exchange further promotes retention, making the bay head a major depositional zone (Kang et al., 2024).

Situated at the head of Deep Bay, the Core of the Mai Po Reserve (CMPR, 22.49°N, 114.03°E) is influenced by inflows from the Shenzhen River in the north and the Shan Pui River in the south (Fig. 1B). The Mai Po Nature Reserve, which encompasses CMPR, has been designated as a "Wetland of International Importance" under the Ramsar Convention since 1995 (Agriculture, Fisheries and Conservation Department, 2011). As a strictly protected zone within the reserve, CMPR has restricted human activity and is actively managed to prevent the spread of invasive mangrove species. A total of seven mangrove species have been recorded in the CMPR, including *Aegiceras corniculatum*, *Excoecaria agallocha*, *Avicennia marina*, *Bruguiera gymnorhiza*, *Nypa fruticans*, *Kandelia obovata*, and *Sonneratia apetala*, the latter being an introduced species (Agriculture, Fisheries and Conservation Department, 2011).

2.2. Sampling and hydrological monitoring sites

In May 2024, two sediment cores were collected in the central sector of the CMPR, where mangrove expansion is strictly restricted by human-imposed boundaries, using PVC tubes with a diameter of 7 cm. This area was selected to characterize sediment dynamics across a fringe–interior gradient. Specifically, MP1 (22.4947°N 114.0285°E) was taken from the

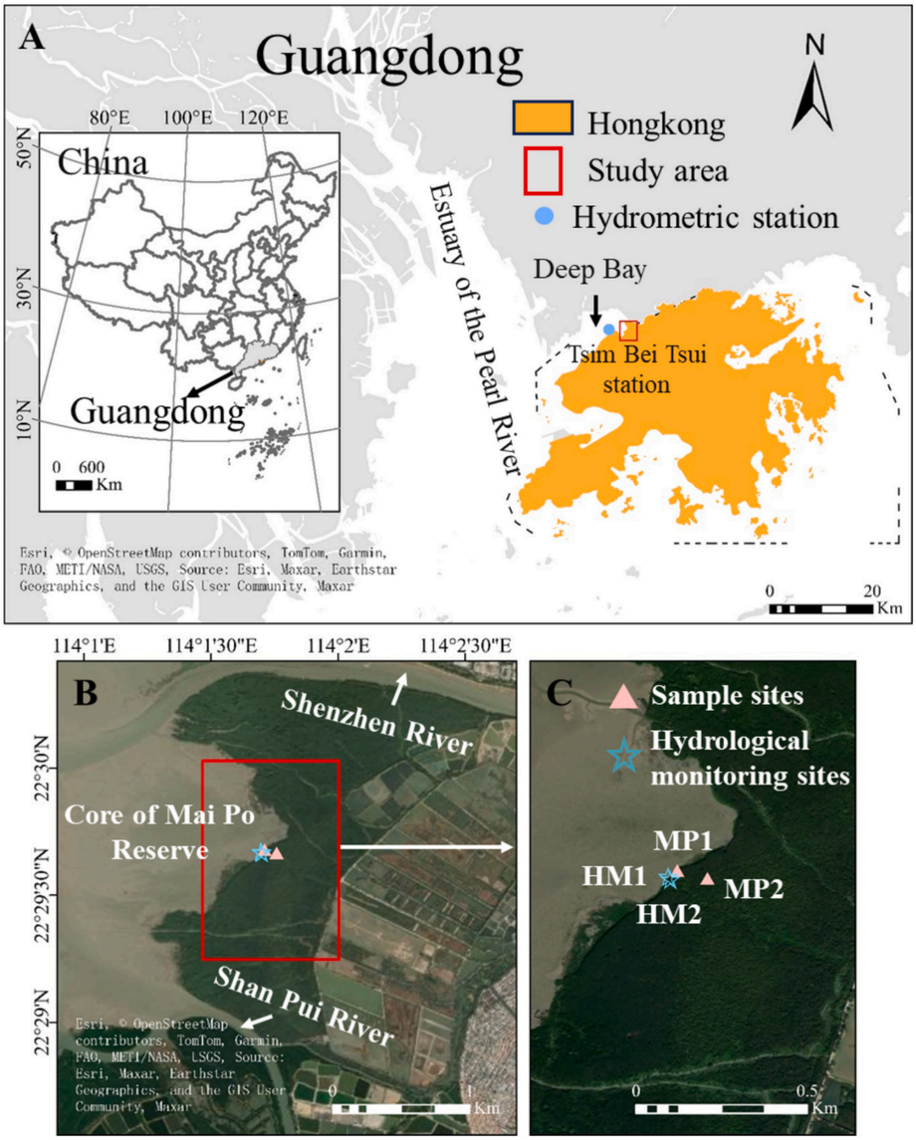

Fig. 1. (A) Location of Deep Bay within China (B); Overview of the study area (C); Sampling sites MP1 and MP2, and hydrological monitoring stations HM1 and HM2.

unvegetated mudflat near the seaward edge of the mangroves, and MP2 (22.4945°N 114.0292°E) was obtained from a densely vegetated mangrove area (Fig. 1C). The two sampling sites, which are approximately 85 m apart, are located along a vegetation gradient from the unvegetated mudflat (MP1) to a densely vegetated mangrove area (MP2). Four surface sediment samples were collected at approximately 40 m intervals along the transect between MP1 and MP2 to characterize horizontal sediment variability, with MP1 corresponding to the second sampling point along the transect. The adjacent mangrove stands are dominated by *Kandelia obovata* (Jia et al., 2014). The core from MP1 was 94 cm long, whereas sediment retrieval at MP2 was limited to 50 cm due to dense roots and compact soils. Both cores were sectioned at 2 cm intervals immediately after collection.

Two hydrological monitoring sites were established to assess hydrodynamic variations between the unvegetated mudflat and the mangrove fringe, with HM1 being designated on the mudflat, while HM2 being designated near the mangrove fringe (Fig. 1C). HM1 and HM2 were spaced 10 m apart. To minimize disturbance to the sediment coring sites, the two hydrological stations were positioned to the south of the sampling locations (Fig. 1C). At both HM1 and HM2, wave gauges (RBRsolo[3]; RBR Ltd., Canada) were mounted 10 cm above the seabed to record wave height, wave period, and water depth. Measurements were collected at a sampling frequency of 4 Hz over 20-min intervals. In addition, electromagnetic current meters (AEM-USB; ALEC Co., Japan) were installed at each site, positioned 15 cm above the seabed in a downward-facing orientation, to measure current velocity. Only data corresponding to water depths greater than 20 cm were retained for analysis. Furthermore, one optical backscatter sensor (OBS-3 A; D&A Instrument Company, Port Townsend, Washington, USA) was deployed at each site to monitor turbidity. Wave height, water depth, and current velocity were continuously recorded from 22 May to 12 July 2024, whereas turbidity was measured from 22 May to 30 May 2024. The monitoring period corresponds to the transition from the pre-flood to early flood season in Deep Bay and was characterized by semidiurnal tidal forcing under non-extreme conditions. Therefore, the observations reflect typical hydrodynamic and wave conditions in the study area.

2.3. Data sources

The sea level data for the inner Deep Bay were sourced from the Tsim Bei Tsui station of the Hong Kong Observatory (https://www.hko.gov.hk/en/cis/yearlyTide.htm?stn=TBT). Tropical cyclone best track data from 1990 to 2023 were obtained from the International Best Track Archive for Climate Stewardship (Gahtan et al., 2024; https://doi.org/10.25921/82ty-9e16), which provides the most comprehensive global archive of historical tropical cyclone activity (Knapp et al., 2010). All available Landsat time-series images (Collection 2 Level 2) with less than 40% cloud cover from 1987 to July 2025 (Path 121, Row 44–45; Path 122, Row 44) were obtained from Google Earth Engine (GEE; https://earthengine.google.com). The dataset includes Landsat 5 TM, 7 ETM+, 8 OLI, and 9 OLI-2, all featuring a spatial resolution of 30 m and referenced to the WGS84 system and UTM projection. These images underwent standardized preprocessing, including radiometric calibration, atmospheric correction, and geometric correction, following the USGS Collection 2 Level 2 protocols (Dwyer et al., 2018). During preprocessing, cloud and cloud shadow pixels were identified and removed using the Quality Assessment band. Additionally, the Surface Reflectance Atmospheric Opacity band was employed to reduce atmospheric interference, ensuring data consistency for mangrove mapping.

2.4. Sediment characterization

Sediment grain sizes were measured using a laser particle size analyzer (Beckman Coulter LS 13320) following pretreatment to remove carbonates with 10% HCl and organic matter with 10% H_2O_2. Sodium hexametaphosphate was used as a dispersing agent. The measurement error was within 5%. Based on standard classification, the MP1 and MP2 sediments were divided into three fractions: clay (<4 μm), silt (4–63 μm), and sand (>63 μm). Clay and silt fractions were combined and referred to as fine-grained sediments.

2.5. Sediment dating with ^{210}Pb

The sediment samples were first oven-dried and then ground. For each depth interval, a known mass of the homogenized sample was transferred into a 15 mL capped round-bottom centrifuge tube, sealed with parafilm. The precise weight of each sample was recorded. To allow for the establishment of secular equilibrium between ^{226}Ra and its daughter isotopes ^{214}Pb and ^{214}Bi, the samples were stored for at least three weeks prior to analysis. Gamma-ray measurements were performed using a high-purity germanium (HPGe) gamma-ray spectrometer (ORTEC, USA; model GWL-120-15-XLB-AWT), with a relative efficiency of 35% and an energy resolution of 1.96 keV at 1332 keV. The activity of ^{226}Ra was determined indirectly by measuring the γ emissions of its short-lived daughters, ^{214}Pb and ^{214}Bi, at 351.9 keV and 609.3 keV, respectively. Excess ^{210}Pb (^{210}Pbex) was calculated by subtracting supported ^{210}Pb, assumed to be in equilibrium with ^{226}Ra, from total ^{210}Pb activity (Mabit et al., 2014).

To better characterize sediment accumulation in mangrove areas, sedimentation fluxes were estimated using the Constant Rate of Supply (CRS) model (Sanders et al., 2016). The CRS model was applied based on the following equations, as described by Appleby and Oldfield (1978) and Sánchez-Cabeza and Ruiz-Fernández (2012):

$$A(i) = \int_{m_{i+1}}^{\infty} C_i dm \tag{1}$$

$$A(0) = \sum_{i=1}^{n} C_i m_i \tag{2}$$

$$t(i) = \frac{1}{\lambda} ln \frac{A(0)}{A(i)} \tag{3}$$

$$r(i) = \frac{\lambda A(i)}{C(i)} \tag{4}$$

where A (i) denotes the accumulative activity of ^{210}Pbex below layer i (Bq m^{-2}), C_i is the ^{210}Pbex activity in Layer i (Bq/kg), m_i denotes the mean mass depth of Section i (kg m^{-2}), r(i) is the MAR of each layer (g cm^{-2} y^{-1}), and n represents the last section.

2.6. Mangrove classification and shoreline analysis

The Continuous Change Detection and Classification (CCDC) algorithm, as proposed by Zhu and Woodcock (2014), was employed to analyze mangrove dynamics. The CCDC method fits harmonic, trend, and break models to all available clear observations at the pixel level for monitoring gradual and abrupt changes (Zhu and Woodcock, 2014; Zhu et al., 2015). It reduces the dependency on fully cloud-free composite images by utilizing the entire time series of Landsat data. The long-term temporal modeling of CCDC has the potential to reduce the impact of tidal variability, allowing for more accurate detection of persistent mangrove changes. Sample points were collected in 1990, 1995, 2000, 2005, 2010, 2015, 2020 and 2024. Classification performance was evaluated using overall accuracy and the Kappa coefficient, with results exceeding 0.93 and 0.90, respectively, indicating high classification reliability.

To quantify the change rate of mangrove shoreline, this study employed the Digital Shoreline Analysis System (DSAS), a tool developed by the United States Geological Survey (USGS). DSAS is an extension for the ArcGIS platform designed to analyze time-series shoreline vector data and calculate rates of shoreline change (Himmelstoss et al., 2021). Shoreline vectors derived from remote sensing imagery acquired in 1990, 1995, 2000, 2005, 2010, 2015, 2020 and 2024 were standardized and subsequently input into DSAS for analysis. A total of 540 transects were automatically generated at 10 m intervals perpendicular to the baseline. To characterize the long-term migration trend of the mangrove front, the Weighted Linear Regression method was applied. The WLR approach fits a regression line to all shoreline positions in the time series and provides statistically derived migration rates along with their associated confidence intervals. In this study, these regression-based confidence intervals were used to represent the uncertainty of shoreline change.

3. Results

3.1. Horizontal variations in hydrodynamics and sediment characteristics

During the hydrodynamic monitoring period (22 May–12 July 2024), four spring–neap tidal cycles (Tsn1–Tsn4) were identified over the CMPR, during which a consistent pattern of water depth variation was observed from the bare flat (HM1) to the inner edge of the mangrove fringe (HM2). Turbidity measurements (22–30 May 2024) encompassed nine consecutive tidal cycles (T1–T9). Mean water depth decreased from 0.32 m at HM1 to 0.22 m at HM2 along the landward transect (Fig. 2A), representing an approximately 31% reduction. The maximum wave height (Hmax) showed only minor differences between HM1 and HM2, with average values of 0.006 m and 0.004 m, respectively, with observed maxima of 0.11 m and 0.07 m. Overall, both sites were characterized by low-energy conditions, with Hmax generally below 0.1 m and mean current velocities of 0.05 m/s (Fig. 2 BCE).

At the horizontal level, despite the weak flow conditions, turbidity exhibited the greatest contrast between the two sites. The average NTU at HM1 was 94.56, while at HM2 it was significantly lower at 36.98, representing a sharp decrease of approximately 61% (Fig. 2D). At T6, turbidity exhibited the greatest reduction, with the average NTU decreasing from 147.38 at HM1 to 40.74 at HM2, representing a maximum decrease of approximately 72% (Fig. 2D). In the same spatial framework, surface sediments also exhibited a clear spatial coarsening trend. Mean grain size showed little change from 6.60 φ at the outer site to 6.32 φ at MP1, followed by a rapid decrease to 4.63 φ at the intermediate site, and then a more gradual change to 4.32 φ at MP2 (Fig. 3).

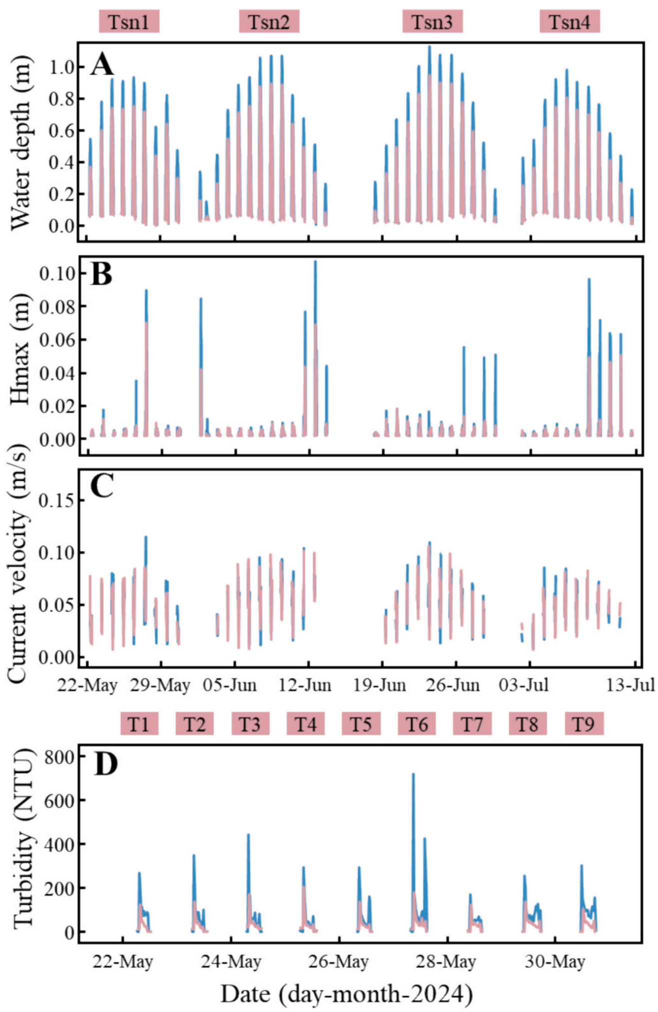

Fig. 2. (A) Water depth, (B) Hmax (maximum wave height), (C) current velocity, (D) turbidity measured at HM1 (blue) and HM2 (pink); NTU is the unit of turbidity. Tsn1 denotes an incomplete spring–neap cycle due to initial deployment timing. (For interpretation of the references to colour in this figure legend, the reader is referred to the web version of this article.)

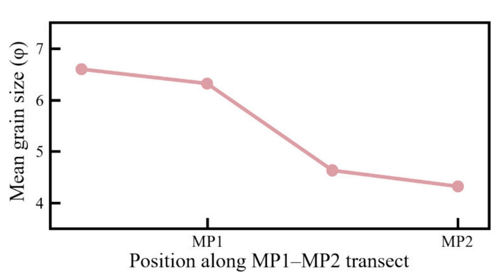

Fig. 3. Spatial variation in mean grain size along the MP1–MP2 transect across a seaward-to-landward mangrove fringe-to-interior gradient, with MP1 representing the second sampling point and adjacent sampling points spaced approximately 40 m apart.

3.2. *Vertical sediment characteristics*

The vertical distributions of clay, silt, and sand contents in sediment cores MP1 and MP2 with depth are shown in Fig. S1. Fine-grained sediments account for approximately 80% of the total in MP1, whereas in MP2 they make up about 55%, indicating a relatively coarser composition. At comparable depths, MP1 generally contains a higher proportion of fine-grained sediments than MP2 (Fig. S1). Specifically, clay content ranges from 4.90% to 37.57% (MP1) and 3.23% to 23.58% (MP2), respectively; silt ranges from 39.60% to 78.87% (MP1) and 23.27% to 71.05% (MP2); and sand varies between 2.59% and 55.50% (MP1) and 9.20% to 75.07% (MP2) (Fig. S1). The results of the *t*-test support this observation, showing a significant difference in grain size distribution between the two cores at the 5% significance level (Fig. S2). Consistent with the t-test results, the mean grain size of MP1 is 5.86 φ (medium silt), whereas MP2 exhibits a coarser texture with a mean of 4.59 φ (coarse silt) (Fig. S2).

The vertical variations in mean grain size further highlight the contrasting depositional environments at MP1 and MP2. Both cores exhibit oscillatory patterns in grain size with depth, but the magnitude and timing of changes differ between the two sites. At MP1, two distinct coarsening events are observed: after 2006, the mean grain size decreased from 6.58 φ to 5.80 φ, and it further coarsened to 5.20 φ after 2017 (Fig. 4). In contrast, MP2 exhibits a different temporal pattern. From 1996 onward, the mean grain size increased markedly from 3.35 φ to 5.14 φ, indicating a pronounced fining trend. However, after 2017, a clear coarsening event occurred, with the mean grain size decreasing from 5.14 φ to 3.96 φ (Fig. 4).

3.3. *Vertical sedimentation process*

The total activities of ^{210}Pb, ^{226}Ra, and ^{210}Pbex ranged from 123.87 to 81.36, 52.93 to 38.64, and 71.18 to 33.53 Bq/kg in MP1, respectively; and from 155.76 to 86.05, 62.29 to 50.03, and 102.05 to 23.77 Bq/kg in MP2, respectively. In MP1, the ^{210}Pbex exhibits a generally decreasing trend with notable fluctuations, particularly above the 30 cm depth. In contrast, MP2 shows a more stable decline, with a slight fluctuation only observed at around 29 cm (Fig. S3).

The CRS-derived age–depth profiles indicate that MP1 spans 1999 to 2024 and MP2 spans 1994 to 2023 (Fig. 5). The mean deposition rates were 1.21 g cm^{-2} yr^{-1} for MP1 and 0.54 g cm^{-2} yr^{-1} for MP2. For MP1, a marked decline occurred between 1999 and 2016, with rates sharply decreasing from 1.40 to 0.94 g cm^{-2} yr^{-1} and a mean value of 1.12 g cm^{-2} yr^{-1}. After 2016, the rates rebounded and stabilized around 1.31 g cm^{-2} yr^{-1} (Fig. 5A). For MP2, the sedimentation rates remained relatively stable without abrupt shifts. Overall, a gradual decline is observed from 0.60 g cm^{-2} yr^{-1} in 1994 to 0.42 g cm^{-2} yr^{-1} in 2023, indicating a persistent but modest decrease throughout the record (Fig. 5B).

4. Discussion

4.1. *Impacts of mangrove dynamics*

Mangroves serve as highly efficient sediment traps, exhibiting a strong capacity for capturing and retaining both suspended sediments and particulate matter (Kathiresan, 2003). The complex above-ground root systems of mangroves promote the settling and retention of sediments, with higher root density further enhancing their capacity to trap suspended particles (Liu et al., 2022). In particularly, under weak hydrodynamic conditions (Fig. 2), a substantial amount of sediment is intercepted and retained by mangroves (Woodroffe et al., 2016), which is a primary reason for the low MAR observed at MP2. As sediments pass through the dense and well-managed mangrove fringe of CMPR under low hydrodynamic conditions, a large proportion is trapped, leading to a sharp decrease in turbidity (Fig. 2D). Fine-grained sediments readily undergo flocculation, forming aggregates with larger effective volumes that enhance settling efficiency. The increased particle size raises the likelihood of collision with the complex aerial root structures of mangroves, while root-induced flow attenuation further promotes preferential interception and stable retention of these flocs (Kamal et al., 2017). As the mangrove fringe serves as the first interception zone for incoming suspended sediments, fine flocculated particles are preferentially trapped at the forest edge before being transported further

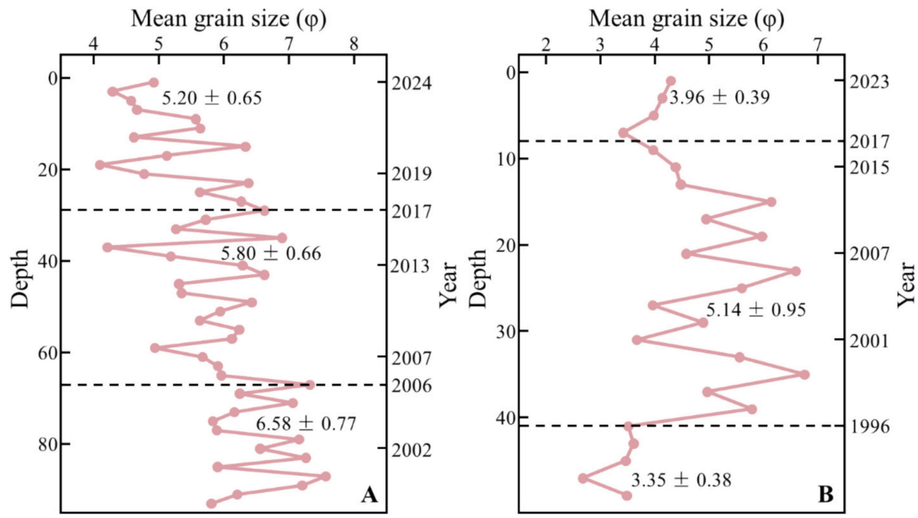

Fig. 4. Mean grain size profiles with depth and over time at (A) MP1 and (B) MP2.

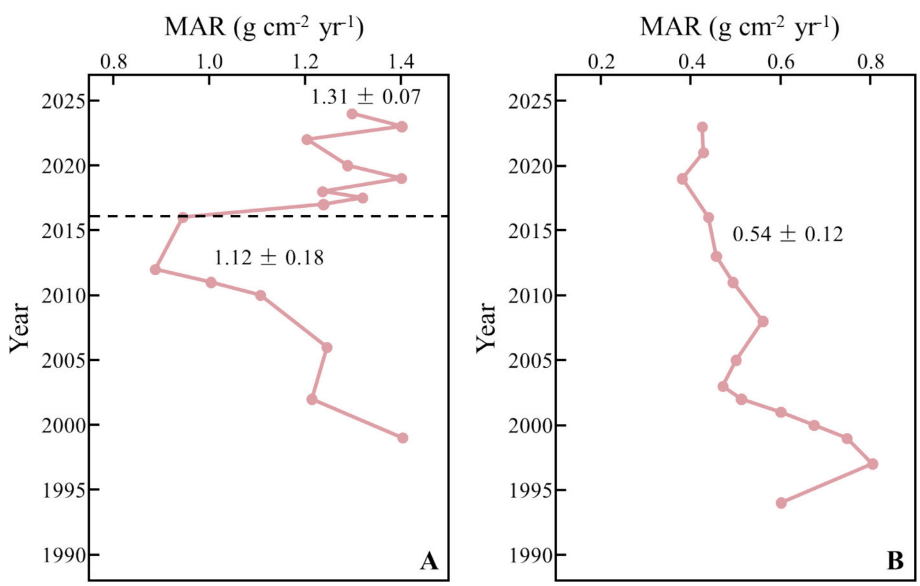

Fig. 5. Mass accumulation rate (MAR) of (A) MP1 and (B) MP2.

landward, resulting in the significantly finer grain size observed at MP1 compared to MP2 (Fig. S2).

Mangrove development depends on the availability of suitable intertidal mudflat substrates. By analyzing and tracking the spatial dynamics of mudflats in the CMPR, we found an overall expansion trend, with only a slight retreat observed in the central sector at a maximum rate of 4.12 m yr^{-1} (Fig. S4). The extensive and generally stable mudflat areas provide a suitable and persistent substrate for mangrove expansion. Reported elevation data indicate that since 2002, most mudflat surfaces in the CMPR have remained above 0 m and experienced slight further accretion by 2018 (Fig. S5), suggesting that the intertidal platform has maintained elevations favorable for mangrove establishment and expansion. The mangrove area in the CMPR rapidly expanded by approximately 127.27 ha from 1990 to 2011, increasing by 104% relative to its initial extent, with an average growth rate of 6.06 ha yr^{-1} (Fig. 6I). This growth was primarily concentrated in the northern and southern sections of the reserve (Fig. 6AE). Consistent with this spatial pattern, the rate of seaward shoreline advancement was also heterogeneous. High expansion rates occurred in both the northern and southern sections, which directly receive sediment input from the Shenzhen River and Shan Pui River (Fig. S6). In contrast, the sampling site at Transect 256 exhibited a much lower expansion rate of 1.22 m yr^{-1}, far below the overall mean of 12.54 m yr^{-1} (Fig. S6). Consequently, no substantial shoreline shift occurred along this transect, and MP1 and MP2 remained located at the mangrove fringe and within the mangrove forest, respectively, throughout the observation period (Fig. 6AH). After 2005, mangroves in the northern section expanded rapidly seaward, with the shoreline advancing closer to the open water relative to the sampling site (Fig. 6DE). This positional shift facilitated earlier interception of river-borne sediments and enhanced the trapping of fine-grained particles (Fig. S6). As a result, sediments at MP1 underwent a pronounced coarsening after 2006 (Fig. 4A). Owing to its persistent location within the mangrove interior, MP2 primarily received secondary sediments that had already been filtered by the mangrove fringe. Consequently, the grain-size composition at MP2 remained relatively stable despite the rapid seaward expansion of the northern mangroves, while being consistently coarser than that of MP1 during the same period (Fig. 4). Meanwhile, the continued mangrove expansion in the northern section further impeded tidal sediment transport. From 1990 to 2011, both MP1 and MP2 exhibited a declining trend in MAR, which can be attributed to

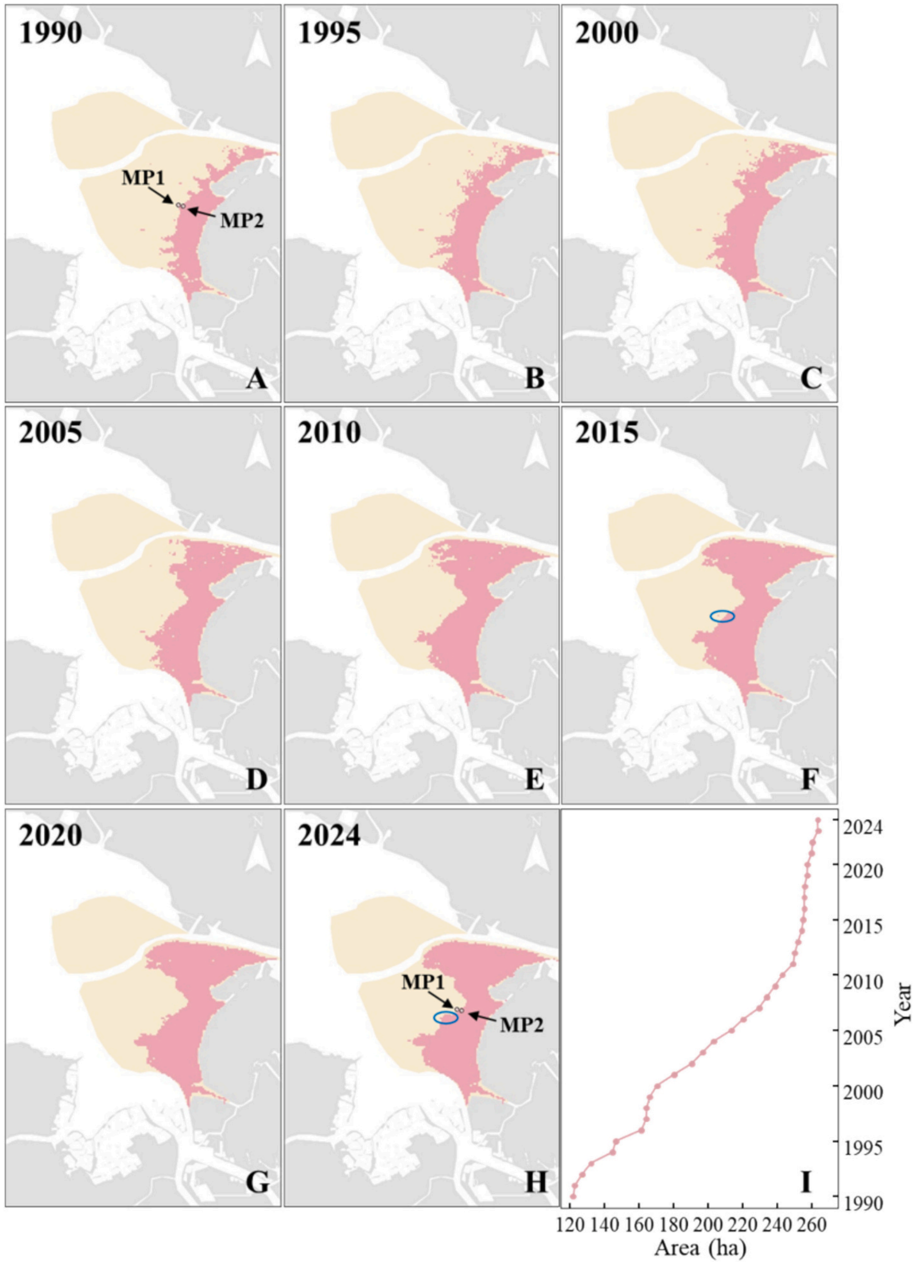

Fig. 6. (A-H): Mangrove distribution in the Mai Po Reserve from 1990 to 2024; (I) Temporal changes in mangrove forest area in the Mai Po Reserve from 1990 to 2024. Pink represents mangrove forest, and yellow represents tidal flat. (For interpretation of the references to colour in this figure legend, the reader is referred to the web version of this article.)

a decrease in sediment availability during this period (Fig. 5). Since 2015, the mangrove area has increased by only 8.39 ha, with expansion observed in the central section (Fig. 6FH), while the mangrove shoreline has progressively extended toward MP1, favoring an increase in MAR at this site. However, the rapid rebound of MAR observed at MP1 after 2016 exceeds what would be expected from the relatively slow shoreline advancement alone, suggesting that additional factors, such as increased sediment supply or local hydrodynamic changes, may have further enhanced carbon accumulation.

4.2. Impacts of local hydrodynamics on mangrove sedimentation

Mangrove fringe zones are often subjected to stronger tidal currents and wave action, which promote sediment erosion and reworking (Norris et al., 2021; Sánchez-Núñez et al., 2019). However, as a distinctive semi-enclosed, low-energy bay, Deep Bay exhibits higher sedimentation rates at its mangrove fringes. The geomorphology of Deep Bay is characterized by a narrow entrance that gradually widens inland, with the channel width increasing from 4667 m to 7056 m (Fig. S7), leads to a marked reduction in hydrodynamic energy toward the mangrove zone. Such low-energy conditions provide a relatively stable setting for sediment deposition within the mangrove system and are conducive to sediment retention at the mangrove fringe (Horstman et al., 2014; Chen et al., 2018). In this study, the fringe tidal flat at MP1, located in the semi-enclosed and weak hydrodynamic energy environment of Deep Bay, exhibited a higher mass accumulation rate (MAR) than the interior site MP2 across all observed periods. Even the lowest MAR at MP1 (0.89 g cm^{-2} yr^{-1} in 2012) was higher than the highest MAR recorded at MP2 (0.80 g cm^{-2} yr^{-1} in 1997) (Fig. 5). Similar patterns of higher sedimentation rates at mangrove fringes have also been reported in other bays (Xu, 2020; Brunskill et al., 2002).

Weak hydrodynamic conditions in Deep Bay are primarily reflected in current velocities and wave heights that typically remain below 0.1 m/s and 0.1 m, respectively (Fig. 2 BCE). In the fringe zone, low current velocities promote sediment deposition by increasing the residence time of suspended particles near mangrove roots. The greater variability in surface radionuclide activities at MP1 indicated a relatively stronger tidal influence compared to MP2 (Fig. S3). At the same time, small yet persistent waves intermittently resuspend bottom sediments, increasing their residence time in the water and further promoting deposition. These processes collectively contribute to the consistently high MAR observed at MP1. In contrast, the mangrove interior (MP2) exhibits markedly lower sedimentation rates, primarily due to limited sediment supply and insufficient hydrodynamic forcing (Cinco-Castro et al., 2022). Turbidity drops sharply after passing through the fringe zone (Fig. 2D), and water depth decreases by approximately 27–50% upon entering the mangrove fringe (Fig. 2A), continuing to decline toward MP2. This results in significantly shorter inundation durations at MP2 relative to MP1, which not only limits hydrodynamic exchange but also reduces the opportunity for suspended sediments to settle and interact with the mangrove substrate. In the upper intertidal zone, the progressive reduction in water depth increases bottom friction and further constrains hydrodynamic energy (Le Hir et al., 2000), thereby limiting the landward transport of suspended sediments. Collectively, the reduced inundation time and sediment availability likely account for the lower MAR observed at MP2 compared to MP1.

The large-scale channel regulation project of the Shenzhen River, initiated in 1995, involved comprehensive straightening, widening, and deepening of the river channel (He and Ye, 2010). This artificial modification significantly reduced hydraulic resistance, thereby enhancing tidal penetration upstream and facilitating the landward transport of marine fine-grained sediments into the mangrove zone. This altered hydrodynamic pattern ultimately led to the pronounced fining trend observed at MP2 (Fig. 4B). More recently, the substantial seaward expansion of the northern mangroves exerted a marked influence on the local hydrodynamic conditions within the sampling area. Following 2015, mangroves in the northern section had reached their expansion limit, with dense stands occupying the river margins and creating a relatively enclosed spatial configuration (Fig. 6). Consequently, river discharge was increasingly obstructed by these riparian mangroves, which substantially reduced its influence on the central section. Dense mangrove stands attenuated overbank runoff flows, reducing runoff-driven hydrodynamic influence and allowing tidal currents to dominate the central mangrove interior, thereby promoting more effective sediment transport toward the interior (Fig. 7). Notably, a distinct sedimentary platform emerged in the northern part of the sampling area in 2018 (Fig. S8BC), where sediments preferentially accumulated. Furthermore, sediments do not simply pass through the mangrove forest; rather, their movement is significantly disrupted by the structural complexity of the mangroves, which slows, redirects, or promotes the deposition of suspended particles (Jiang et al., 2025). As a result, influenced by the prevailing southward flow, a substantial portion of the sediments is likely transported along the mangrove fringe toward downstream areas (Fig. S7), ultimately leading to a sudden increase in MAR at MP1 (Fig. 5). Between 2019 and 2024, the sedimentary platform further developed and extended seaward, positioning itself closer to the open water than MP1. The mangroves rapidly responded by colonizing the formed sedimentary platform, which was subsequently followed by the formation of additional sedimentary platforms and continued seaward expansion of the mangrove forest (Fig. S8D-F). Correspondingly, the MAR at MP1 responded rapidly, rising sharply from 0.94 g cm^{-2} yr^{-1} in 2016 and stabilizing at an average of 1.31 g cm^{-2} yr^{-1}, representing an increase of 39% (Fig. 5A).

4.3. Impacts of extreme events

Hong Kong is particularly susceptible to typhoons (Abbas et al., 2020), which exert significant and complex influences on sedimentation rates in mangrove ecosystems. Typhoons can bring substantial external sediment through storm surges, while intensified waves reshape sediment distribution by enhancing resuspension and transport, leading to either increased deposition or erosion (Castañeda-Moya et al., 2020; Li et al., 2022). In particular, typhoon events typically cause sediment coarsening, as finer particles are transported away, leaving behind coarser fractions (Ma et al., 2019).

Considering that typhoons within an 80 km radius of the study area are most likely to affect the mangrove region (Amaral et al., 2023), we focused on these events to evaluate their potential impact on sediment dynamics. Between 1990 and 2023, the average maximum wind speed of typhoons affecting the study area was 52 kt. Notably, two extreme events occurred in 2017 and 2023, with maximum wind speeds of 101 kt and 103 kt, respectively (Fig. 8A). The generally low-energy hydrodynamic conditions in Deep Bay, characterized by shallow waters and strong bottom friction, limit sediment resuspension under typical or weak typhoon events, so that minor storms have only a limited effect on local sediment dynamics (Liu et al., 1998). In contrast, extreme typhoons produce sufficiently strong wave and current forces to overcome these low-energy constraints, mobilizing and flushing large quantities of

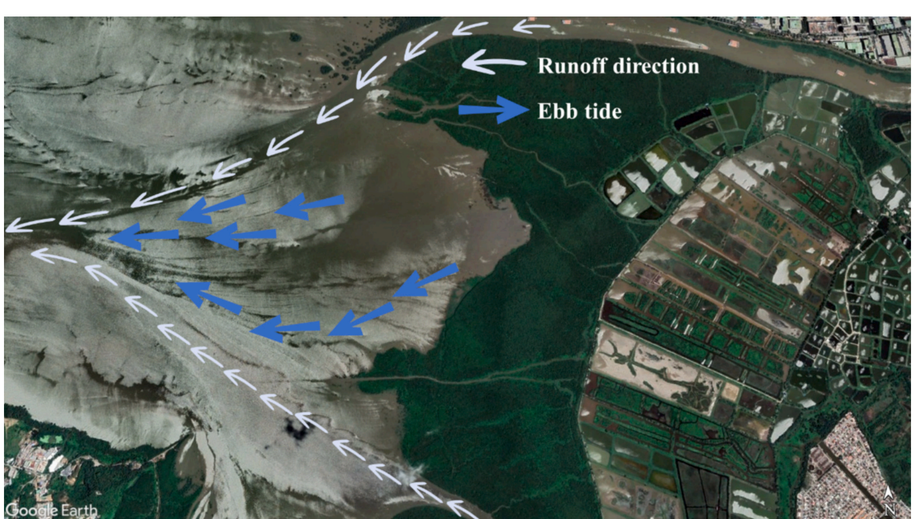

Fig. 7. Diagram showing the interaction among river discharge, tidal currents and mangrove vegetation. Source: Google Earth, 2021 (© Google, 2023, https://www.google.com/earth/).

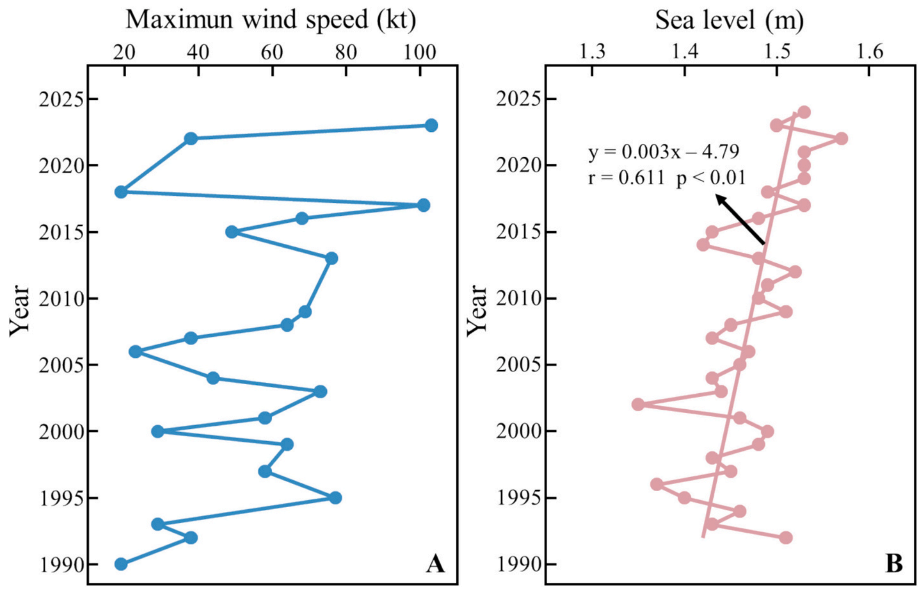

Fig. 8. (A) Annual maximum wind speed of typhoon affecting the study area during 1990–2023; (B) Annual variations of the mean sea level (1990–2024).

fine sediments offshore, while intense winds may additionally remove exposed fine particles through aeolian transport (Ma et al., 2019). At the same time, the enhanced hydrodynamic energy facilitates the transport and redistribution of coarser particles within the system, leading to pronounced sediment coarsening at both MP1 and MP2, as evidenced by grain-size shifts after 2017 (Fig. 4). The weak baseline hydrodynamics also slow the recovery of sediment grain size after such events, prolonging the influence of typhoon-induced changes.

4.4. Sedimentary mode summary of the CMPR mangrove ecosystem

A conceptual understanding of sedimentation in the CMPR mangrove system provides valuable insights into how mangroves regulate sediment dynamics in low-energy bay environments (Fig. 9). The seaward fringe is primarily composed of young and sparsely distributed mangroves, whereas the landward interior is dominated by mature stands with higher vegetation density (Fig. S8). Mangrove trunks, branches, and foliage effectively attenuate tidal currents and enhance sediment trapping (Dasgupta et al., 2019). The vegetation structure of young mangroves is relatively simple, with thinner trunks and sparser canopies, resulting in lower sediment-trapping efficiency compared to mature stands (Hu et al., 2022). Along the fringe–interior gradient, mangroves at the seaward fringe are generally younger and structurally

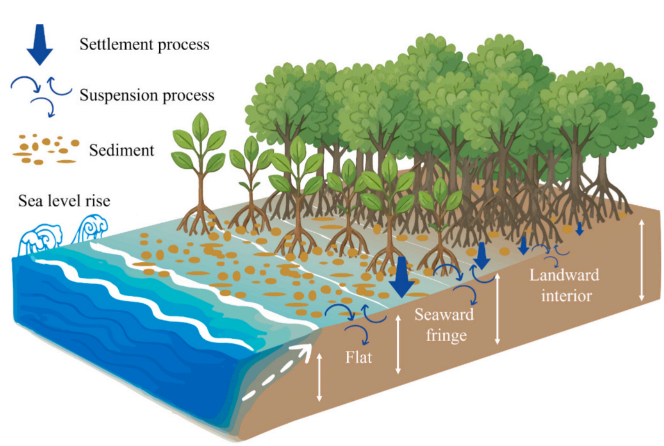

Fig. 9. Schematic diagram of sedimentation processes in the CMPR mangrove system.

less complex, resulting in weaker sediment retention capacity compared to the more mature stands in the landward interior. However, mangroves in the seaward fringe are situated in zones of active sedimentation, where they directly interact with tidal flows and incoming sediments. This enables mangroves intercept primary sediment inputs delivered by tides, leading to high sedimentation rates and the formation of elevated sediment platforms. Fine suspended sediments are preferentially captured at the fringe during this process, producing a clear coarsening trend in surface sediment grain size from the fringe toward the interior (Fig. 3). Once these platforms reach a certain height, mangroves rapidly colonize the newly accreted areas, thereby facilitating repeated seaward expansion (Fig. S8D-F). As residual sediments continue migrating landward, their availability progressively declines after passing through successive belts of mature mangroves. Consequently, landward mangroves receive reduced sediment inputs and become increasingly reliant on limited and redistributed sediment sources.

Meanwhile, global sea-level rise has led to the submergence of intertidal zones, thereby influencing sedimentation rates (Jiang et al., 2020). In intertidal mangrove zones, surface elevation typically increases from the seaward fringe to the landward interior. Consequently, seaward mangroves occupy lower elevations and experience more frequent and prolonged tidal inundation (Ellison et al., 2022). These extended submergence periods enhance their sedimentation potential (Bomer et al., 2020b), resulting in significantly higher sediment accumulation rates compared to interior mangroves. Such elevated sedimentation in the seaward fringe allows mangroves to keep pace with sea-level rise, thereby supporting their vertical accretion and long-term resilience (Sasmito et al., 2016). In Hong Kong, sea level has been rising at a relatively slow rate of approximately 0.003 m yr^{-1}, which is insufficient to exert a discernible impact on sedimentation rates in the CMPR in the short term (Fig. 8B). However, sea-level rise is projected to accelerate markedly under future climate change scenarios (Mengel et al., 2016), potentially elevating tidal water levels within bays and intensifying tidal currents, which in turn may enhance the frequency and extent of sediment resuspension (Passeri et al., 2016). In regions characterized by weak hydrodynamic energy, such as the study area, these changes may facilitate greater offshore sediment input, thereby contributing to increased MAR at both MP1 and MP2.

4.5. Comparison with other mangrove wetlands and global applications

Mangroves are widely distributed across diverse coastal settings, encompassing estuarine, bay, open-coast, and lagoonal environments (Worthington et al., 2020). The contrasting hydrodynamic conditions among these settings lead to distinct sediment distribution patterns (Xu, 2020; Bomer et al., 2020a; Jiang et al., 2024). Under weak hydrodynamic conditions, the seaward mangrove fringe effectively traps substantial sediment, whereas interior mangroves exhibit reduced sedimentation rates and relatively coarser grain sizes. This pattern is evident in Deep Bay, which, as a semi-enclosed bay, typically exhibits weak hydrodynamic energy (Li et al., 2023; Han et al., 2022), and is similarly observed in mangrove wetlands across Oceania and Asia (Table S3), including Missionary Bay and Tieshan Bay (Brunskill et al., 2002; Xu, 2020). In mesoscale hydrodynamic settings, numerous cases, including the Sundarbans mangrove forest, Jinhai Bay, Pearl Bay, and the Cananéia mangroves, show that although sedimentation rates at the seaward fringe are relatively high, the grain size at the fringe is coarser than within the interior (Table S3). This coarsening trend arises because tidal currents or wave energy transported finer sediments landward into the mangrove interior, but remain coarse particle at the mangrove fringe to retain (Bomer et al., 2020a; Xu, 2020; Sanders et al., 2010a). With the transition to high-energy hydrodynamic conditions at the fringe, this sorting process can shift to active erosion, while the interior, protected by dense vegetation, generally continues to accumulate sediment (Le Nguyen and Luong, 2019). Additionally, riverine sediment inputs can further enhance overall mangrove sedimentation (Jiang et al., 2024).

In the compiled dataset comparing sedimentation rates across mangrove wetlands in Oceania, Asia, and the Americas, all documented cases indicate that mangrove-mediated sedimentation occurs primarily at the seaward fringe (Table S3). However, this conclusion cannot be considered robust under high-energy hydrodynamic conditions. For example, a Vietnamese mangrove study documented that although energetic tidal inflows eroded 2.5 mm at the fringe and left coarser deposits, sediment supplied during ebb tides produced a net accretion of 11.9 mm, still exceeding that of the interior (Norris et al., 2021; Norris et al., 2017). Comparisons of sedimentation between mangrove fringes and interiors in energetic environments are exceedingly scarce, providing insufficient evidence for a generalized pattern. This paucity of data likely reflects that, under high-energy conditions, severe fringe erosion and pronounced hydrodynamic forcing at the seaward margin may render sediment cores from the fringe unsuitable for the relevant analyses.

As Table S2 indicates, sediment accumulation patterns in mangrove wetlands are regulated by the dominant hydro-sedimentary regime. Systems primarily controlled by tidal forcing, river discharge, or wave energy exhibit distinct hydrodynamic characteristics and sediment delivery pathways. Within this framework, the CMPR mangrove can be characterized as a tide-dominated, low-energy system that is nevertheless strongly influenced by the Shenzhen River through both sediment supply and hydrodynamic modification. The 1995 channel regulation reduced hydraulic resistance (He and Ye, 2010), thereby enhancing tidal penetration upstream and facilitating the landward transport of fine-grained sediments into the mangrove, which ultimately led to the pronounced fining trend observed at MP2 (Fig. 4B). Meanwhile, the rapid northward expansion of mangroves progressively obstructed overbank runoff and reduced the direct influence of fluvial surface flows, thereby reinforcing the dominant role of tidal processes in regulating sediment distribution (Fig. 7).

4.6. Methodological strengths, limitations, and future perspectives

A combination of long-term sediment chronologies, short-term hydrodynamic monitoring, and event-scale analysis provides a multi-scale perspective on mangrove sediment dynamics. By coupling ^{210}Pb-derived mass accumulation rates with in situ measurements of waves, currents, and turbidity, we directly link process-based hydrodynamics to stratigraphic records, thereby strengthening causal interpretation. The incorporation of time-series remote sensing and shoreline change analysis further relates vegetation expansion to sediment redistribution, while the identification of typhoon signals enables differentiation between background sedimentation and episodic disturbances. Together, this integrative framework enhances the robustness of process–response interpretation across temporal scales. Nevertheless, several limitations should be acknowledged. Hydrodynamic observations were conducted over a relatively short, non-extreme period and may not fully capture interannual variability or extreme-event responses. Sediment cores were collected at two representative sites along a fringe–interior gradient; although these sites reflect contrasting depositional settings, they do not resolve the full spatial heterogeneity of the mangrove platform. In addition, the absence of direct elevation measurements limits quantitative assessment of vertical accretion relative to sea-level rise.

Future studies should incorporate high-resolution topographic surveys and surface elevation measurements to better constrain vertical accretion dynamics. Coupled hydrodynamic–sediment transport modeling would further clarify sediment redistribution under varying tidal regimes and vegetation configurations. Beyond simulating sediment transport processes, such models can generate diagnostic variables, including bed shear stress, flow velocity, and sediment fluxes, which are directly relevant for interpreting sediment transport pathways and depositional patterns within the study area. In particular, bed shear stress is a key control on erosion and deposition processes and can provide important mechanistic insight into the observed spatial variability in sediment distribution. Moreover, integrating sediment dynamics with detailed biogeochemical analyses, particularly organic carbon burial efficiency and source apportionment, would advance understanding of how hydrodynamic modification regulates blue-carbon sequestration in mangrove ecosystems. In addition, the potential influence of small-scale anthropogenic structures, such as floating birdwatching hides, on local hydro-sedimentary processes remains largely unexplored and may warrant further investigation.

5. Conclusion

Situated within a semi-enclosed bay, the Mai Po Reserve is recognized as an internationally important wetland, renowned for its ecological value and landscape significance. Investigating sediment grain size and sediment mass accumulation rate in this region is essential for understanding how mangroves regulate sediment dynamics under low-energy hydrodynamic conditions. This study examines temporal variations in MAR within the Core of the Mai Po Reserve and explores the underlying drivers of these changes. The key findings are summarized as follows:

(1) From 1990 to 2024, sediment grain size and MAR exhibited distinct temporal patterns across the sampling sites. At the seaward mangrove fringe (MP1), sediment grain size experienced two episodes of coarsening, with the mean decreasing from 6.58φ to 5.80φ in 2006 and further to 5.20φ in 2017. In the interior mangrove zone (MP2), sediments first became finer, increasing from 3.35 φ in 1996 to 5.14 φ, and then coarsened to 3.96 φ after 2017. MAR at MP1 showed a pronounced decline, dropping from 1.40 g cm^{-2} yr^{-1} in 1999 to 0.94 g cm^{-2} yr^{-1} in 2016, but subsequently rebounded sharply and stabilized at a relatively high level. In contrast, MAR at MP2 exhibited a steady decline throughout the study period, with an average value of 0.54 g cm^{-2} yr^{-1}. Overall, MAR at MP1 consistently exceeded that at MP2, averaging approximately 2.2 times higher.

(2) From 1996 onward, local hydrodynamic changes induced by Shenzhen River regulation led to early-stage sediment fining at MP2. Mangrove expansion was the primary driver of sediment

coarsening and the sharp increase in sediment accumulation rates along the seaward fringe. After 2005, the rapid seaward expansion of mangroves enabled them to intercept tidal and fluvial sediments, with finer particles preferentially retained. This process resulted in sediment coarsening at MP1 after 2006, while the interior site (MP2) was less affected. As mangroves progressively encroached into river channels, they altered the dominant hydrodynamic regime, enhancing tidal influence. By 2018, a well-developed sediment platform had formed north of the sampling site, where sediments were more readily deposited. Southward-flowing tidal currents subsequently transported sediments laterally along the mangrove fringe, which contributed to the pronounced increase in MAR at MP1 after 2016.

(3) The weak hydrodynamic conditions, characterized by a mean significant wave height below 0.1 m and an average current velocity below 0.1 m/s, led to reduced inundation duration and a substantial decline in sediment concentration as water moved from the mangrove fringe to the interior. This mechanism is a key reason for the MAR at MP1 was approximately 2.2 times higher than that at MP2. Furthermore, two typhoon events after 2017 caused pronounced sediment coarsening at both MP1 and MP2, whereas sea-level rise exerted no significant impact during the study period.

Our findings indicate that flow velocities on the unvegetated mudflats at the mangrove fringe have declined to levels insufficient to induce erosion, thereby favoring sediment deposition. These results fill a critical evidence gap concerning the hydrodynamic conditions supporting high sedimentation rates at the mangrove fringe. At the ecosystem scale, sedimentation exhibits a pattern of seaward aggradation and landward stabilization, with much higher accumulation rates at the fringe than in the interior, enhancing the system's capacity to adapt to climate change. Given these findings, we emphasize the need for continued investigation into mangrove sedimentation mechanisms under accelerating sea-level rise.

CRediT authorship contribution statement

Weiming Li: Writing – review & editing, Writing – original draft, Visualization. **Zhijun Dai:** Writing – review & editing, Writing – original draft, Visualization, Supervision, Project administration, Methodology, Funding acquisition, Formal analysis, Conceptualization. **Xuefei Mei:** Writing – review & editing, Writing – original draft, Visualization, Supervision, Methodology, Formal analysis, Conceptualization. **Jiejun Luo:** Writing – review & editing, Visualization, Methodology, Data curation. **Wenjun Zeng:** Writing – review & editing, Visualization, Methodology, Data curation. **Ping Zhang:** Writing – review & editing, Visualization, Software, Methodology. **Ran Chen:** Writing – review & editing, Methodology, Formal analysis. **Jinping Cheng:** Writing – review & editing, Visualization, Methodology, Formal analysis, Conceptualization, Funding acquisition.

Declaration of competing interest

The authors declare that they have no known competing financial interests or personal relationships that could have appeared to influence the work reported in this paper.

Acknowledgments

This research was supported by Shanghai International Science and Technology Cooperation Fund Project (23230713800; 24230740100; 23590780200), and Croucher Foundation Visitorship for PRC Scholars (2025/26) provided funding support to Dr. Jinping Cheng at the Education University of Hong Kong to host Prof. Xuefei Mei from the East China Normal University.

Appendix A. Supplementary data

Supplementary data to this article can be found online at https://doi.org/10.1016/j.margeo.2026.107839.

Data availability

The in situ hydrodynamic data used in this study are publicly and can be accessed via: https://doi.org/10.5281/zenodo.19217975

References

Abbas, S., Nichol, J.E., Fischer, G.A., Wong, M.S., Irteza, S.M., 2020. Impact assessment of a super-typhoon on Hong Kong's secondary vegetation and recommendations for restoration of resilience in the forest succession. Agric. For. Meteorol. 280, 107784. https://doi.org/10.1016/j.agrformet.2019.107784.

Agriculture, Fisheries and Conservation Department, 2011. Mai Po Inner Deep Bay Ramsar Site management plan executive summary. Agriculture, Fisheries and Conservation Department, Hong Kong.

Allison, M.A., Nittrouer, C.A., Faria Jr., L.D.C., 1995. Rates and mechanisms of shoreface progradation and retreat downdrift of the Amazon river mouth. Mar. Geol. 125 (3–4), 373–392. https://doi.org/10.1016/0025-3227(95)00020-Y.

Alongi, D.M., 2014. Carbon cycling and storage in mangrove forests. Annu. Rev. Mar. Sci. 6 (1), 195–219. https://doi.org/10.1146/annurev-marine-010213-135020.

Alongi, D.M., 2025. Global meta-analysis of mangrove primary production: implications for carbon cycling in mangrove and other coastal ecosystems. Forests 16 (5), 747. https://doi.org/10.3390/f16050747.

Amaral, C., Poulter, B., Lagomasino, D., Fatoyinbo, T., Taillie, P., Lizcano, G., Roman-Cuesta, R.M., 2023. Drivers of mangrove vulnerability and resilience to tropical cyclones in the North Atlantic Basin. Sci. Total Environ. 898, 165413. https://doi.org/10.1016/j.scitotenv.2023.165413.

Anu, K., Sneha, V.K., Busheera, P., Muhammed, J., Augustine, A., 2024. Mangroves in environmental engineering: harnessing the multifunctional potential of nature's coastal architects for sustainable ecosystem management. Results Eng. 21, 101765. https://doi.org/10.1016/j.rineng.2024.101765.

Appleby, P.G., Oldfield, F., 1978. The calculation of lead-210 dates assuming a constant rate of supply of unsupported 210Pb to the sediment. Catena 5 (1), 1–8. https://doi.org/10.1016/S0341-8162(78)80002-2.

Bomer, E.J., Wilson, C.A., Elsey-Quirk, T., 2020a. Process controls of the live root zone and carbon sequestration capacity of the Sundarbans mangrove forest, Bangladesh. Science 2 (3), 54. https://doi.org/10.3390/sci2030054.

Bomer, E.J., Wilson, C.A., Hale, R.P., Hossain, A.N.M., Rahman, F.A., 2020b. Surface elevation and sedimentation dynamics in the Ganges-Brahmaputra tidal delta plain, Bangladesh: evidence for mangrove adaptation to human-induced tidal amplification. Catena 187, 104312. https://doi.org/10.1016/j.catena.2019.104312.

Brunskill, G.J., Zagorskis, I., Pfitzner, J., 2002. Carbon burial rates in sediments and a carbon mass balance for the Herbert River region of the Great Barrier Reef continental shelf, North Queensland, Australia. Estuar. Coast. Shelf Sci. 54 (4), 677–700. https://doi.org/10.1006/ecss.2001.0852.

Castañeda-Moya, E., Rivera-Monroy, V.H., Chambers, R.M., Zhao, X., Lamb-Wotton, L., Gorsky, A., Gaiser, E.E., Troxler, T.G., Kominoski, J.S., Hiatt, M., 2020. Hurricanes fertilize mangrove forests in the Gulf of Mexico (Florida Everglades, USA). Proc. Natl. Acad. Sci. 117 (9), 4831–4841. https://doi.org/10.1073/pnas.1908597117.

Chen, Y., Li, Y., Thompson, C., Wang, X., Cai, T., Chang, Y., 2018. Differential sediment trapping abilities of mangrove and saltmarsh vegetation in a subtropical estuary. Geomorphology 318, 270–282. https://doi.org/10.1016/j.geomorph.2018.06.018.

Cinco-Castro, S., Herrera-Silveira, J., Comín, F., 2022. Sedimentation as a support ecosystem service in different ecological types of mangroves. Front. For. Glob. Change 5, 733820. https://doi.org/10.3389/ffgc.2022.733820.

Dasgupta, S., Islam, M.S., Huq, M., Huque Khan, Z., Hasib, M.R., 2019. Quantifying the protective capacity of mangroves from storm surges in coastal Bangladesh. PLoS One 14 (3), e0214079. https://doi.org/10.1371/journal.pone.0214079.

Duarte, C.M., Cebrián, J., 1996. The fate of marine autotrophic production. Limnol. Oceanogr. 41 (8), 1758–1766. https://doi.org/10.4319/lo.1996.41.8.1758.

Dung, B., Thang, D., Hau, D., Trang, N., Cuong, L., Khanh, N., Thang, D., Nam, P., Bac, V., Ha, N., 2023. Temporal trends of sediment accumulation in the Xuan Thuy Natural Wetland Reserve (Ba Lat coastal area of the Red River, Vietnam) and implications for future coastal wetland development. Wetl. Ecol. Manag. 31 (3), 419–433. https://doi.org/10.1007/s11273-023-09925-4.

Dwyer, J.L., Roy, D.P., Sauer, B., Jenkerson, C.B., Zhang, H.K., Lymburner, L., 2018. Analysis ready data: enabling analysis of the Landsat archive. Remote Sens. 10 (9), 1363. https://doi.org/10.3390/rs10091363.

Ellison, J.C., Buffington, K.J., Thorne, K.M., Gesch, D., Irwin, J., Danielson, J., 2022. Elevations of mangrove forests of Pohnpei, Micronesia. Estuar. Coast. Shelf Sci. 268, 107780. https://doi.org/10.1016/j.ecss.2022.107780.

Feher, L.C., Osland, M.J., Anderson, G.H., Vervaeke, W.C., Krauss, K.W., Whelan, K.R.T., Balentine, K.M., Tiling-Range, G., Smith III, T.J., Cahoon, D.R., 2020. The long-term effects of hurricanes Wilma and Irma on soil elevation change in Everglades mangrove forests. Ecosystems 23, 917–931. https://doi.org/10.1007/s10021-019-00446-x.

Gahtan, J., Knapp, K.R., Schreck III, C.J., Diamond, H.J., Kossin, J.P., Kruk, M.C., 2024. International Best Track Archive for Climate Stewardship (IBTrACS) Project, Version

4r01 (subset: ALL). NOAA National Centers for Environmental Information. https://doi.org/10.25921/82ty-9e16 (accessed 4 September 2025).
Gijsman, R., Horstman, E.M., Swales, A., MacDonald, I.T., Bouma, T.J., van der Wal, D., Wijnberg, K.M., 2024. Mangrove forest drag and bed stabilisation effects on intertidal flat morphology. Earth Surf. Process. Landf. 49, 1117–1134. https://doi.org/10.1002/esp.5758.
Han, X., Kuang, C., Li, Y., Song, W., Qin, R., Wang, D., 2022. Numerical modeling of a green tide migration process with multiple artificial structures in the western Bohai Sea, China. Appl. Sci. 12, 3017. https://doi.org/10.3390/app12063017.
He, Y., Ye, X.Y., 2010. Analysis of water-sediment variation after regulation project phase 1 and phase 2 in Shenzhen River. Pearl River 31, 10–13 (in Chinese with English abstract).
Himmelstoss, E.A., Henderson, R.E., Kratzmann, M.G., Farris, A.S., 2021. Digital Shoreline Analysis System (DSAS) version 5.1 user guide. . U.S. Geological Survey Open-File Report 2021–1091. doi:. https://doi.org/10.3133/ofr20211091.
Hong Phuoc, V.L., Massel, S.R., 2006. Experiments on wave motion and suspended sediment concentration at Nang Hai, Can Gio mangrove forest, Southern Vietnam. Oceanologia 48, 23–40.
Hongwiset, S., Rodtassana, C., Poungparn, S., Umnouysin, S., Suchewaboripont, V., 2022. Synergetic roles of mangrove vegetation on sediment accretion in coastal mangrove plantations in Central Thailand. Forests 13, 1739. https://doi.org/10.3390/f13101739.
Horstman, E.M., Dohmen-Janssen, C.M., Narra, P.M.F., van den Berg, N.J.F., Siemerink, M., Hulscher, S.J.M.H., 2014. Wave attenuation in mangroves: a quantitative approach to field observations. Coast. Eng. 94, 47–62. https://doi.org/10.1016/j.coastaleng.2014.08.005.
Hu, J., Loh, P.S., Pradit, S., Le, T.P.Q., Oeurng, C., Mohamed, C.A.R., Guo, J., 2022. Assessing the effect of age and geomorphic setting on organic carbon accumulation in high-latitude human-planted mangroves. Forests 13, 105. https://doi.org/10.3390/f13010105.
Jia, M., Zhang, Y., Wang, Z., Song, K., Ren, C., 2014. Mapping the distribution of mangrove species in the Core Zone of Mai Po Marshes Nature Reserve, Hong Kong, using hyperspectral data and high-resolution data. Int. J. Appl. Earth Obs. Geoinf. 33, 226–231. https://doi.org/10.1016/j.jag.2014.06.006.
Jia, M., Wang, Z., Wang, C., Mao, D., Zhang, Y., 2019. A new vegetation index to detect periodically submerged mangrove forest using single-tide Sentinel-2 imagery. Remote Sens. 11, 2043. https://doi.org/10.3390/rs11172043.
Jiang, L., Gerkema, T., Idier, D., Slangen, A., Soetaert, K., 2020. Effects of sea-level rise on tides and sediment dynamics in a Dutch tidal bay. Ocean Sci. 16, 307–321. https://doi.org/10.5194/os-16-307-2020.
Jiang, Z., Sanders, C.J., Xin, K., Wang, F., Sheng, N., Xiong, Y., 2024. Increasing carbon and nutrient burial rates in mangroves coincided with coastal aquaculture development and water eutrophication in NE Hainan, China. Mar. Pollut. Bull. 199, 115934. https://doi.org/10.1016/j.marpolbul.2023.115934.
Jiang, W., Huang, Z., Dai, Z., Luo, J., Zeng, W., Liang, X., 2025. Attenuation of hydro-sediment dynamics progradation over mangrove wetland. J. Geophys. Res. Oceans 130, e2024JC021531. https://doi.org/10.1029/2024JC021531.
Kamal, S., Warnken, J., Bakhtiyari, M., Lee, S.Y., 2017. Sediment distribution in shallow estuaries at fine scale: in situ evidence of the effects of three-dimensional structural complexity of mangrove pneumatophores. Hydrobiologia 803, 121–132. https://doi.org/10.1007/s10750-017-3178-3.
Kang, Y., Lu, C., Gao, S., Wu, Y., 2024. Riverbed erosion-deposition dynamics and driving mechanisms in Shenzhen Bay, 2002–2020. Adv. Water Sci. 35, 947–959 (In Chinese with English abstract).
Karimi, Z., Abdi, E., Deljouei, A., Cislaghi, A., Shirvany, A., Schwarz, M., Hales, T.C., 2022. Vegetation-induced soil stabilization in coastal area: an example from a natural mangrove forest. Catena 216, 106410. https://doi.org/10.1016/j.catena.2022.106410.
Kathiresan, K., 2003. How do mangrove forests induce sedimentation? Rev. Biol. Trop. 51, 355–360.
Knapp, K.R., Kruk, M.C., Levinson, D.H., Diamond, H.J., Neumann, C.J., 2010. The international best track archive for climate stewardship (IBTrACS): unifying tropical cyclone best track data. Bull. Am. Meteorol. Soc. 91, 363–376. https://doi.org/10.1175/2009BAMS2755.1.
Le Hir, P., Roberts, W., Cazaillet, O., Christie, M., Bassoullet, P., Bacher, C., 2000. Characterization of intertidal flat hydrodynamics. Cont. Shelf Res. 20, 1433–1459. https://doi.org/10.1016/S0278-4343(00)00031-5.
Le Nguyen, H.T., Luong, H.P.V., 2019. Erosion and deposition processes from field experiments of hydrodynamics in the coastal mangrove area of Can Gio, Vietnam. Oceanologia 61, 252–264. https://doi.org/10.1016/j.oceano.2018.11.004.
Li, L., Ren, Y., Wang, X.H., Xia, Y., 2022. Sediment dynamics on a tidal flat in macro-tidal Hangzhou Bay during Typhoon Mitag. Cont. Shelf Res. 237, 104684. https://doi.org/10.1016/j.csr.2022.104684.
Li, L., Xu, J., Kong, G., Li, P., Ren, Y., Wang, H., 2023. Hydrodynamics in the tidal flat in semi-enclosed Xiangshan Bay. Front. Mar. Sci. 10, 1073254. https://doi.org/10.3389/fmars.2023.1073254.
Liu, X., Zhao, H., Zheng, D., Ou, X., Chen, X., 1998. The evolution and development—utilization of Shenzhen Bay. Trop. Oceanogr. 7, 48–56 (In Chinese with English abstract).
Liu, X., Liu, H., Chen, L., Wang, X., 2022. Ecological interception effect of mangroves on microplastics. J. Hazard. Mater. 423, 127231. https://doi.org/10.1016/j.jhazmat.2021.127231.
Lovelock, C.E., Cahoon, D.R., Friess, D.A., Guntenspergen, G.R., Krauss, K.W., Reef, R., Rogers, K., Saunders, M.L., Sidik, F., Swales, A., Saintilan, N., Thuyen, L.X., Triet, T., 2015. The vulnerability of Indo-Pacific mangrove forests to sea-level rise. Nature 526, 559–563. https://doi.org/10.1038/nature15538.
Ma, B., Dai, Z., Pang, W., Ge, Z., Li, S., Mei, X., Huang, H., 2019. Dramatic typhoon-induced variability in the grain size characteristics of sediments at a meso-macrotidal beach. Cont. Shelf Res. 191, 104006. https://doi.org/10.1016/j.csr.2019.104006.
Mabit, L., Benmansour, M., Abril, J.M., Walling, D.E., Meusburger, K., Iurian, A.R., Owens, P.N., Blake, W.H., Alewell, C., 2014. Fallout 210Pb as a soil and sediment tracer in catchment sediment budget investigations: a review. Earth Sci. Rev. 138, 335–351. https://doi.org/10.1016/j.earscirev.2014.06.007.
Meijer, K.J., El-Hacen, E.H.M., Govers, L.L., Lavaleye, M., Piersma, T., Olff, H., 2021. Mangrove-mudflat connectivity shapes benthic communities in a tropical intertidal system. Ecol. Indic. 130, 108030. https://doi.org/10.1016/j.ecolind.2021.108030.
Mengel, M., Levermann, A., Frieler, K., Robinson, A., Marzeion, B., Winkelmann, R., 2016. Future sea level rise constrained by observations and long-term commitment. Proc. Natl. Acad. Sci. USA 113, 2597–2602. https://doi.org/10.1073/pnas.1500515113.
Nguyen, T., Ngoc, P., Dung, L., Nguyen, T., Quy, T., Nhuan, M., 2025. Nitrate, ammonium, and phosphate patterns from mangrove sediment cores near extensive aquaculture areas in the Red River Delta, Vietnam. One Ecosyst. 10, e150217. https://doi.org/10.3897/oneeco.10.e150217.
Norris, B.K., Mullarney, J.C., Bryan, K.R., Henderson, S.M., 2017. The effect of pneumatophore density on turbulence: a field study in a *Sonneratia*-dominated mangrove forest, Vietnam. Cont. Shelf Res. 147, 114–127. https://doi.org/10.1016/j.csr.2017.06.002.
Norris, B.K., Mullarney, J.C., Bryan, K.R., Henderson, S.M., 2021. Relating millimeter-scale turbulence to meter-scale subtidal erosion and accretion across the fringe of a coastal mangrove forest. Earth Surf. Process. Landf. 46, 573–592. https://doi.org/10.1002/esp.5047.
Passeri, D.L., Hagen, S.C., Plant, N.G., Bilskie, M.V., Medeiros, S.C., Alizad, K., 2016. Tidal hydrodynamics under future sea level rise and coastal morphology in the Northern Gulf of Mexico. Earth's Future 4, 159–176. https://doi.org/10.1002/2015EF000332.
Pérez, A., Libardoni, B.G., Sanders, C.J., 2018. Factors influencing organic carbon accumulation in mangrove ecosystems. Biol. Lett. 14, 20180237. https://doi.org/10.1098/rsbl.2018.0237.
Pérez, A., Machado, W., Sanders, C.J., 2021. Anthropogenic and environmental influences on nutrient accumulation in mangrove sediments. Mar. Pollut. Bull. 165, 112174. https://doi.org/10.1016/j.marpolbul.2021.112174.
Quadros, A.F., Helfer, V., Nordhaus, I., Reuter, H., Zimmer, M., 2021. Functional traits of terrestrial plants in the intertidal: A review on mangrove trees. Biol. Bull. 241, 123–139. https://doi.org/10.1086/716510.
Sánchez-Cabeza, J.A., Ruiz-Fernández, A.C., 2012. 210Pb sediment radiochronology: an integrated formulation and classification of dating models. Geochim. Cosmochim. Acta 82, 183–200. https://doi.org/10.1016/j.gca.2010.12.024.
Sánchez-Núñez, D.A., Bernal, G., Mancera Pineda, J.E., 2019. The relative role of mangroves on wave erosion mitigation and sediment properties. Estuar. Coasts 42, 2124–2138. https://doi.org/10.1007/s12237-019-00586-2.
Sanders, C.J., Smoak, J.M., Naidu, A.S., Araripe, D.R., Sanders, L.M., Patchineelam, S.R., 2010a. Mangrove forest sedimentation and its reference to sea level rise, Cananeia, Brazil. Environ. Earth Sci. 60, 1291–1301. https://doi.org/10.1007/s12665-009-0269-0.
Sanders, C.J., Smoak, J.M., Naidu, A.S., Sanders, L.M., Patchineelam, S.R., 2010b. Organic carbon burial in a mangrove forest, margin and intertidal mud flat. Estuar. Coast. Shelf Sci. 90, 168–172. https://doi.org/10.1016/j.ecss.2010.08.013.
Sanders, C.J., Smoak, J.M., Waters, M.N., Sanders, L.M., Brandini, N., Patchineelam, S.R., 2012. Organic matter content and particle size modifications in mangrove sediments as responses to sea level rise. Mar. Environ. Res. 77, 150–155. https://doi.org/10.1016/j.marenvres.2012.02.004.
Sanders, C.J., Santos, I.R., Maher, D.T., Breithaupt, J.L., Smoak, J.M., Ketterer, M., Call, M., Sanders, L., Eyre, B.D., 2016. Examining 239+240Pu, 210Pb and historical events to determine carbon, nitrogen and phosphorus burial in mangrove sediments of Moreton Bay, Australia. J. Environ. Radioact. 151, 623–629. https://doi.org/10.1016/j.jenvrad.2015.04.018.
Sarker, S., Masud-Ul-Alam, M., Hossain, M.S., Rahman Chowdhury, S., Sharifuzzaman, S. M., 2021. A review of bioturbation and sediment organic geochemistry in mangroves. Geol. J. 56, 2439–2450. https://doi.org/10.1002/gj.3808.
Sasmito, S.D., Murdiyarso, D., Friess, D.A., Kurnianto, S., 2016. Can mangroves keep pace with contemporary sea level rise? A global data review. Wetl. Ecol. Manag. 24, 263–278. https://doi.org/10.1007/s11273-015-9466-7.
Trégarot, E., Caillaud, A., Cornet, C.C., Taureau, F., Catry, T., Cragg, S.M., Failler, P., 2021. Mangrove ecological services at the forefront of coastal change in the French overseas territories. Sci. Total Environ. 763, 143004. https://doi.org/10.1016/j.scitotenv.2020.143004.
van Maanen, B., Coco, G., Bryan, K.R., 2015. On the ecogeomorphological feedbacks that control tidal channel network evolution in a sandy mangrove setting. In: Proceedings of the Royal Society A: Mathematical, Physical and Engineering Sciences, 471, 20150115. https://doi.org/10.1098/rspa.2015.0115.
Vundavilli, H., Mullarney, J.C., MacDonald, I.T., 2024. The coalescence of two mangrove-lined river plumes and consequences for sediment transport and deposition in a coastal environment. Cont. Shelf Res. 279, 105280. https://doi.org/10.1016/j.csr.2024.105280.
Wang, D., Dai, Z., Long, C., Liang, X., Xiong, Y., Cheng, J., 2025. The serious loss of mangrove forest over the largest delta of Africa, Niger Delta: causes and reasons. Mar. Environ. Res., 107350 https://doi.org/10.1016/j.marenvres.2025.107350.
Woodroffe, C.D., Rogers, K., McKee, K.L., Lovelock, C.E., Mendelssohn, I.A., Saintilan, N., 2016. Mangrove sedimentation and response to relative sea-level rise. Annu. Rev. Mar. Sci. 8, 243–266. https://doi.org/10.1146/annurev-marine-122414-034025.

Worthington, T.A., Zu Ermgassen, P.S.E., Friess, D.A., Krauss, K.W., Lovelock, C.E., Thorley, J., Tingey, R., Woodroffe, C.D., Bunting, P., Cormier, N., Lagomasino, D., Lucas, R., Murray, N.J., Satyanarayana, B., Spalding, M., 2020. A global biophysical typology of mangroves and its relevance for ecosystem structure and deforestation. Sci. Rep. 10, 14652. https://doi.org/10.1038/s41598-020-71194-5.

Xia, Q., Qin, C.Z., Li, H., Huang, C., Su, F.Z., 2018. Mapping mangrove forests based on multi-tidal high-resolution satellite imagery. Remote Sens. 10, 1343. https://doi.org/10.3390/rs10091343.

Xu, H., 2020. Study on sedimentary and carbon burial characteristics and expansion history of typical mangroves in Guangxi. Guangxi University, Nanning (In Chinese with English abstract).

Yang, Y., Chui, T.F.M., 2017. Aquatic environmental changes and ecological implications from the combined effects of sea-level rise and land reclamation in Deep Bay, Pearl River Estuary, China. Ecol. Eng. 108, 30–39. https://doi.org/10.1016/j.ecoleng.2017.08.003.

Yang, Y., Chui, T.F.M., 2021. The role of the Pearl River flow in Deep Bay hydrodynamics and potential impacts of flow variation and land reclamation. J. Hydro Environ. Res. 34, 1–10. https://doi.org/10.1016/j.jher.2020.11.001.

Zhou, Y., Dai, Z., Liang, X., Cheng, J., 2024. Machine learning-based monitoring of mangrove ecosystem dynamics in the Indus Delta. For. Ecol. Manag. 571, 122231. https://doi.org/10.1016/j.foreco.2024.122231.

Zhu, Z., Woodcock, C.E., 2014. Continuous change detection and classification of land cover using all available Landsat data. Remote Sens. Environ. 144, 152–171. https://doi.org/10.1016/j.rse.2014.01.011.

Zhu, Z., Woodcock, C.E., Holden, C., Yang, Z., 2015. Generating synthetic Landsat images based on all available Landsat data: Predicting Landsat surface reflectance at any given time. Remote Sens. Environ. 162, 67–83. https://doi.org/10.1016/j.rse.2015.02.009.